



Future impacts of climate change on inland Ramsar wetlands

Yi Xi ¹, Shushi Peng ¹✉, Philippe Ciais ² and Youhua Chen ³

The 1971 Ramsar Convention promotes wetland conservation worldwide, yet climate change impacts on wetland extent and associated biodiversity are unclear. Hydrological modelling and soil moisture estimates are used to quantify climate change-driven shifts in wetland area across 1,250 inland Ramsar sites. We estimate that net global wetland area expanded during 1980–2014, but 47% of sites experienced wetland loss. By 2100, a net area loss of at least 6,000 km² (about 1%) is projected. The number of sites with area loss over 10% will increase by 19–65% under low emissions, 148–243% under high emissions and -16% with global mean warming of 2 °C relative to 1.5 °C. Sites most vulnerable to shrinkage are located in the Mediterranean, Mexico, Central America and South Africa—all seasonal waterbird migration hotspots. Our findings highlight that climate mitigation is essential for future Ramsar wetlands conservation, in addition to the minimization of human disturbance.

Wetlands are estimated to have been shrinking in the past decades^{1–4}, which may jeopardize their ecosystem services such as water purification, flood control, biodiversity conservation and food supply^{5–8}, and carbon sequestration is sourced from wetlands⁹. To promote the conservation and wise use of wetlands worldwide, the Convention on Wetlands (the Ramsar Convention) was signed in 1971, the only international agreement focused on wetlands. By September of 2018, 2,339 wetlands were designated as Wetlands of International Importance according to nine criteria for Ramsar site designation (Supplementary Table 1). These wetlands are representative, rare or unique and have a specific importance for conserving biological diversity (Supplementary Table 1). Among all of the Ramsar sites, there are 1,352 inland wetlands covering 2 million km², about 15% of the global inland wetland area¹⁰ (Fig. 1a). Regionally, 47% of the inland Ramsar sites are distributed in Europe and 19% in Africa (Extended Data Fig. 1).

Although the Ramsar Convention aims to ensure the conservation of wetlands worldwide, many sites have little or no protection from national governments⁷, and cases of wetland loss or degradation were reported continuously after the establishment of the Convention^{11–13}. For example, a compilation of 189 reports of historical wetland loss from Davidson et al.² shows that the extent of inland wetlands declined by 69–75% during the twentieth century. Wetland loss is also evidenced by satellite-based wetland maps^{14,15}. Among threats of natural wetlands, human disturbance has been regarded as the main driver^{14,16–18}. While the evaluation of the impacts of climate change is limited by the small-scale landscape features of natural wetlands compared with the relatively coarse-resolution spatial grid of global climate fields, hydrological models based on sub-grid topography information have been applied to downscale the climate fields to simulate recent and future wetland dynamics for methane–climate feedbacks^{19–21}. Future wetland dynamics are also closely related to biodiversity conservation and other ecosystem services. Whether future exposure to regional warming and shifts in precipitation will amplify or alleviate Ramsar wetland-area loss^{22–24} and the implications for wetland biodiversity

are still unclear. Thus, evaluating the impacts of climate change for the Ramsar sites and other wetlands is a key priority for inland wetland conservation.

As a means of investigating the past and future changes in wetland area across global inland Ramsar sites, we employ a TOPMODEL-based diagnostic model^{25,26} (more details in Methods and Extended Data Fig. 2). TOPMODEL has been widely applied to downscale mean water-table depth in a catchment or grid scale to wetland fraction on the basis of local topography distribution^{26–30}. In this study, TOPMODEL is forced with monthly gridded water-table depth at 0.5°×0.5° resolution, derived from soil moisture (SM) from GLDAS-Noah v.2.0 for 1980–2014 (ref. ³¹) and from the Climate Model Intercomparison Project Phase 5 (CMIP5)³² climate models for future projections (2006–2100) (Supplementary Discussion 1 and Supplementary Table 2). Then the wetland fractions for each grid cell and each polygon delineating the area of inland Ramsar sites are extracted by downscaling the coarser water table to 500 m×500 m resolution with the compound topographic index (CTI) data³³. Because SM data of CMIP5 and/or regularly flooded wetland (RFW) data are not available for 102 sites located in islands and coastal regions, changes in wetland area in 1,250 sites out of the 1,352 sites are projected here. Key parameters in the model are calibrated with the observation-based RFW map¹⁰ (Methods). The evaluation of the performance of the calibrated model against observed wetland area suggests a root mean square error of less than 3% in most regions and a mean bias of less than 1% across all Ramsar sites (Extended Data Fig. 3). Moreover, given the large discrepancies in wetland estimation across existing wetland maps¹⁰, we compare wetland extent from RFW with three other regional/global wetland maps and evaluate other possible uncertainties in simulating wetland dynamics (Supplementary Discussion 2). For future projection, four representative concentration pathways (RCPs) are considered in this study, and the spread of different climate models provides uncertainties on future wetland-area changes regarding the projection of SM (Methods).

¹Sino-French Institute for Earth System Science, College of Urban and Environmental Sciences, and Laboratory for Earth Surface Processes, Peking University, Beijing, China. ²Laboratoire des Sciences du Climat et de l'Environnement, LSCE/IPSL, CEA-CNRS-UVSQ, Université Paris-Saclay, Gif-sur-Yvette, France. ³CAS Key Laboratory of Mountain Ecological Restoration and Bioresource Utilization & Ecological Restoration and Biodiversity Conservation Key Laboratory of Sichuan Province, Chengdu Institute of Biology, Chinese Academy of Sciences, Chengdu, China. ✉e-mail: speng@pku.edu.cn

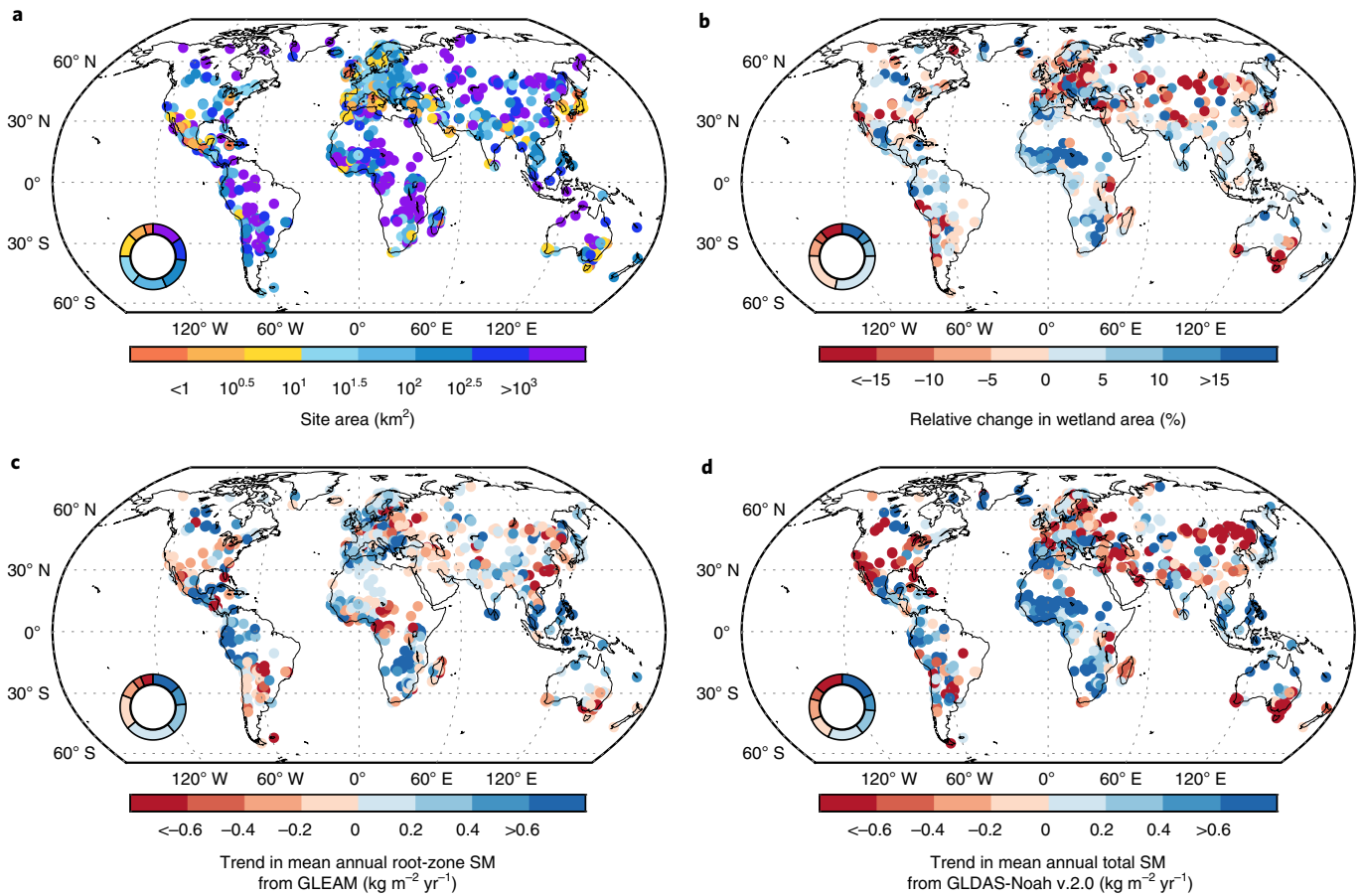


Fig. 1 | Historical change in wetland area and SM across 1,250 inland Ramsar sites. Change from 1980 to 2014 across global inland Ramsar sites. **a**, Spatial patterns of site area. **b**, Simulated change in wetland area on the basis of SM from GLDAS-Noah v.2.0. **c**, Trend in mean annual root-zone SM from GLEAM. **d**, Trend in mean annual total SM from GLDAS-Noah v.2.0.

Historical changes in inland Ramsar wetlands

Historical simulation based on SM from GLDAS-Noah v.2.0 shows that 47% of global inland Ramsar sites suffered a loss of area from 1980 to 2014, one-third of them with an area loss of more than 10% (Fig. 1b). More than 10% wetland gains are found at 16% of the sites, which have large baseline areas (Fig. 1). This results in a net increase in the global area of inland Ramsar wetlands (31,000 km²; ~3%). The increase in wetland area is also reflected in the sign of surface water change from satellite-based data³⁴, which reveals an increase of 9,000 km² in surface water area across the sites for the past three decades (Supplementary Fig. 1). Note that human water use is absent in the land surface model of GLDAS-Noah v.2.0, and wetting of some sites may be overestimated in GLDAS-Noah. Spatially, the distribution of historical wetland change across the Ramsar sites is consistent with independent observations of regional wetting or drying trends (Fig. 1c,d and Supplementary Figs. 1 and 2). Sites with wetland gain are located mainly in regions that are becoming wetter such as Africa, southeastern Europe, Mexico and Central America; these regions also show a consistent increase in mean annual root-zone SM and annual precipitation minus evapotranspiration (P-ET) from the Global Land Evaporation Amsterdam Model (GLEAM, more details in Methods)^{35,36}. Conversely, the sites that experienced a loss in wetland area from our simulation are located mainly in drying regions such as northern Europe, Central Asia and South America. These patterns suggest some level of climate nonlinear control on the trends of wetland area across the globally distributed Ramsar sites.

Future changes in inland Ramsar wetlands

Although the impact of recent climate change on Ramsar wetlands tends to be positive during the past three decades (Fig. 1 and Supplementary Fig. 1), projected future change (Supplementary Figs. 3 and 4) may lead to an important shift^{22,23}. Mean annual temperature over the sites is projected to increase by 0.6–1.8°C under RCP 2.6 and by 2.8–6.0°C under RCP 8.5 by the end of this century relative to the reference period (1981–2000). The canonical patterns of climate models for regional climate changes are reflected across these sites, with a higher warming rate in northern high latitudes than in the tropics, a wetter climate in the high latitudes and a drier climate in tropical, subtropical and Mediterranean regions except in Asia and northern sub-Saharan Africa (Supplementary Figs. 3 and 4). Under RCP 2.6, projected annual precipitation increases by 4–8% by 2100 across sites in northern Europe and Asia and decreases by more than 2% in the Mediterranean, Australia and South Africa. Under RCP 8.5, the annual precipitation changes over the sites are about three times larger in magnitude, both for regions with a decrease and those with an increase. Nonetheless, although more than half of the sites will receive more annual precipitation by 2100 under all RCP scenarios, SM in the grid points containing Ramsar sites may still decrease from higher ET and runoff. The total SM output from CMIP5 models indeed shows a decrease across 79% of inland Ramsar sites by the end of this century under RCP 8.5, with 10% of sites exposed to a moisture decrease larger than 10%, compared with no sites with a decrease larger than 10% under RCP 2.6 (Supplementary Figs. 3 and 4). In terms of the

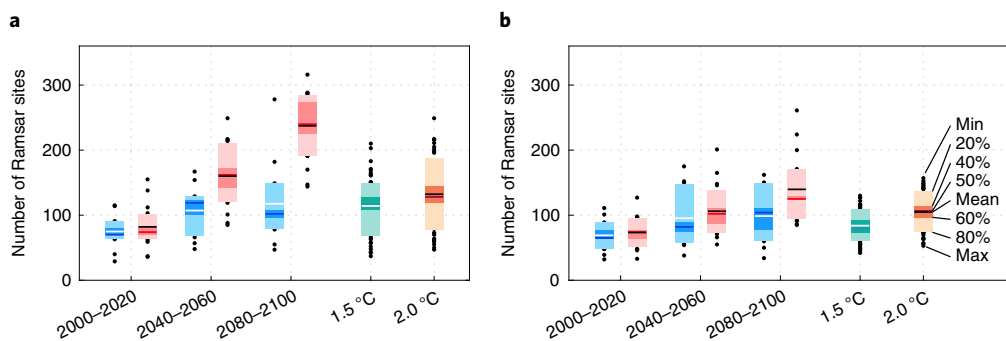


Fig. 2 | Temporal changes in numbers of global inland Ramsar sites with >10% wetland loss/gain through the twenty-first century. a, b. The first three paired boxes denote projected numbers of sites with >10% wetland loss (a) or gain (b) under RCP 2.6 (13 models; blue boxes) and RCP 8.5 (19 models; red boxes) for the epochs of 2000–2020, 2040–2060 and 2080–2100, respectively, and the last two boxes are for a global warming of 1.5°C and 2°C. The black dots indicate projections from individual models. The whiskers and boxes indicate numbers of sites with a >10% wetland change agreed by one model (min), 20%, 40%, 50%, 60%, 80% and all (max) models, as well as projections from the CMIP5 ensemble mean (the white or black lines).

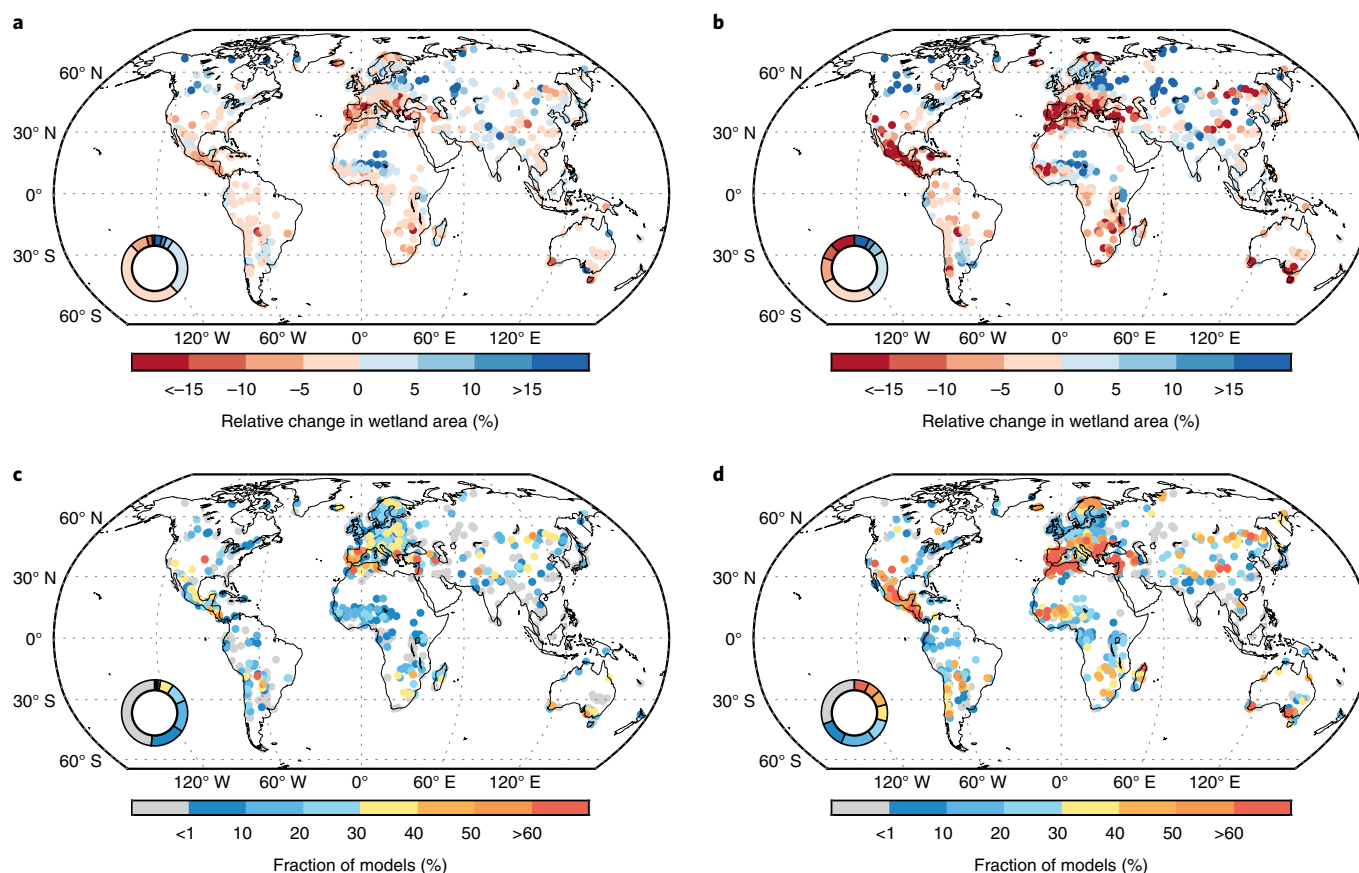


Fig. 3 | Spatial distributions of change in wetland area across global inland Ramsar sites by 2100 and the uncertainties. a, b. Projected change in wetland area for 2081–2100 relative to the reference period 1981–2000 under RCP 2.6 (13 models) (a) and RCP 8.5 (19 models) (b) from the CMIP5 ensemble across global inland Ramsar sites. **c, d.** Fraction of the models agreeing on the >10% wetland loss for each Ramsar site under RCP 2.6 (c) and RCP 8.5 (d).

nonlinear relationship between wetland fraction and $SM^{26,30,37}$, even a small reduction in SM may have a sizeable impact on the future wetland area of Ramsar sites. In this study, we address this question by applying a TOPMODEL-based diagnostic model to each site, forced by bias-corrected SM output from CMIP5 climate models under the four RCP scenarios, which allows us to estimate the uncertainty from the spread of climate models and the signal from different scenarios in the impact analysis (Methods).

For future change in global inland Ramsar sites, we first examine wetland-area losses (Fig. 2 and Supplementary Fig. 5). Under a low warming level of RCP 2.6, the numbers of sites projected to have a wetland loss larger than 10% (N_{-10}) will increase by 48%, with an inter-quartile range (IQR) of 35% between now and the middle of the century, and then stabilize because in the RCP 2.6 scenario, atmospheric CO_2 and global climate warming stabilize after the mid-century. By contrast, N_{-10} increases dramatically by 107% (IQR

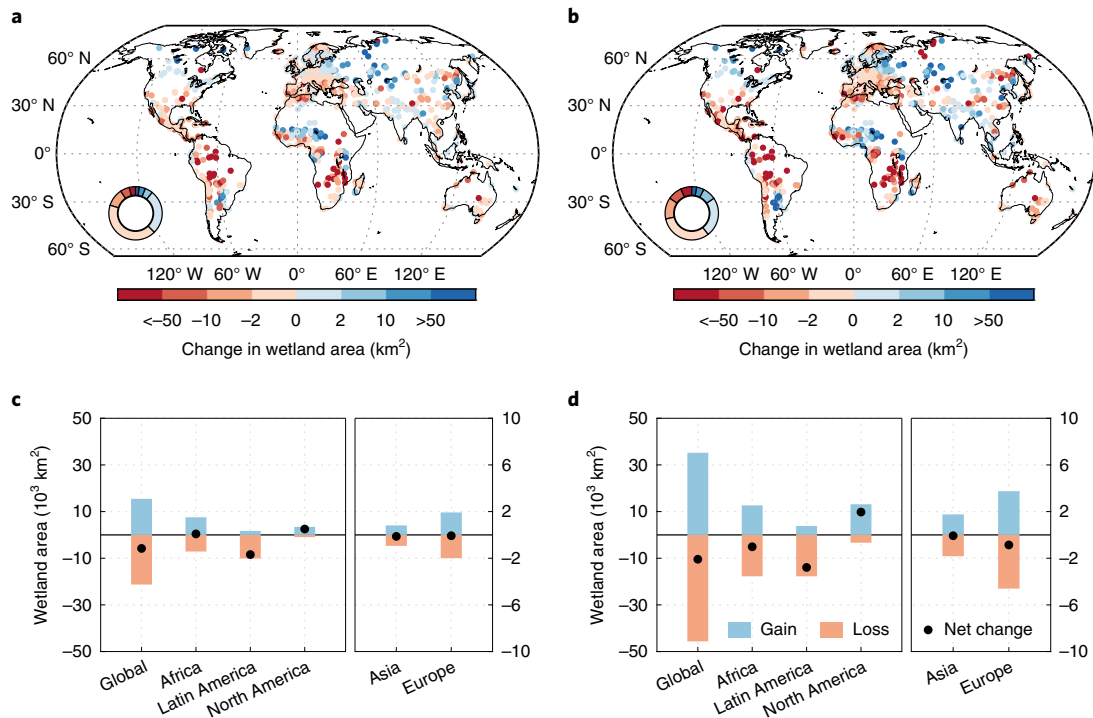


Fig. 4 | Change in absolute wetland area across global inland Ramsar sites and five continents by 2100. a,b, Spatial patterns of projected absolute change in wetland area for 2081–2100 relative to the reference period 1981–2000 under RCP 2.6 (13 models) (**a**) and RCP 8.5 (19 models) (**b**) from the CMIP5 ensemble across global inland Ramsar sites. **c,d**, Projected CMIP5 ensemble mean change in absolute wetland area globally and for five continents (Africa, Latin America, North America, Asia and Europe) under RCP 2.6 (**c**) and RCP 8.5 (**d**). Oceania is not shown here because the total wetland area in the continent accounts for less than 1.5% of global Ramsar wetland area.

68%) by the mid-century and by 215% (IQR 95%) by the end of this century under the high warming level of RCP 8.5. Although there are substantial differences in projected SM from the CMIP5 climate models, 80% of the CMIP5 models consistently predict an over 131% increase in N_{-10} from the beginning to the end of this century. Similar temporal changes in numbers of Ramsar sites are also found when using different cut-offs (Extended Data Fig. 4). As a result, by the end of this century, 80% of climate models indicate that at least 191 sites will experience an area loss of more than 10% under RCP 8.5, against only 78 sites under RCP 2.6, while 35 sites will have a severe area loss larger than 50% (N_{-50}) for RCP 8.5, compared with only 9 sites under RCP 2.6 (Extended Data Fig. 5). Globally, gross loss of wetland area of Ramsar sites by the end of this century doubles between RCP 2.6 (21,000 km², IQR 23,000 km²) and RCP 8.5 (46,000 km², IQR 55,000 km²). The global gross loss area is less than 5% under the four RCP scenarios; however, the sites with loss concentrate in the Mediterranean, Mexico and Central America, South America and southern African regions, which have a much higher percentage loss than all global sites (Fig. 3). Furthermore, comparing the wetland change under two special scenarios—that is, the global warming of 1.5°C and 2°C above the reference period (1981–2000)—we find that limiting the global warming to 1.5°C would avoid 123 sites being exposed to a more than 10% area decrease under RCP 8.5, whereas a 2°C warming would avoid 105 sites to remain below this loss threshold (Fig. 2). This indicates a substantially avoided impact of climate change on wetland area for 1.5°C and 2°C warming compared with RCP 8.5.

Second, we investigate wetland-area gains. Similar to wetland losses, the number of inland Ramsar sites with a wetland gain larger than 10% (N_{+10}) also shows an increasing trend from the beginning to the end of this century, but with a smaller increase (46% with an IQR of 73% under RCP 2.6 and 103% with an IQR of 104% under

RCP 8.5). The global value of N_{+10} is almost equal to that of N_{-10} at the beginning of this century when the climate forcing of the four RCP scenarios is not very differentiated (Fig. 2 and Supplementary Fig. 5). By the middle of the century, N_{-10} surpasses N_{+10} under all scenarios. By the end of the century, N_{-10} is 92% (IQR 96%; 98 sites, IQR 95 sites) larger than N_{+10} under RCP 8.5, indicating that the losses will clearly dominate over gains (Fig. 2). The sites with wetland gain cannot compensate the shrinking sites because the patterns of wetland gains and losses show strong regional differences (Figs. 3 and 4 and Supplementary Figs. 6 and 7), and the Ramsar sites in different regions have different ecosystem services according to the criteria for Ramsar site designation (Supplementary Table 1). By the end of the century, those expanding sites are distributed mainly in northern Europe and northern sub-Saharan Africa, while those parts with a wetland loss will be in the Mediterranean, Mexico and Central America, South America and southern African regions. Thus, the sites that are diagnosed to have a historical wetland-area gain in the Mediterranean, Mexico and Central America (Fig. 1b) will be likely to face a wetland-area shrinkage. The spatial patterns of wetland gain or loss by 2100 from the CMIP5 ensemble mean are similar among the four RCP scenarios, but the regional contrasts between wetland gains and losses are amplified in scenarios that have a higher global warming level (Figs. 3 and 4 and Supplementary Figs. 6 and 7). Furthermore, the degree of model agreement for a wetland loss larger than 10% will double at 481 sites going from RCP 2.6 to RCP 8.5 (Fig. 3c,d and Supplementary Fig. 6c,d). The increased model agreement is also found with four other cut-offs (Supplementary Fig. 8). This indicates that with stronger climate warming, a more consistent loss signal emerges from the spread of the climate models.

At the continental scale, the projected multimodel mean N_{-10} increases by 109% to 386% across all five continents under RCP

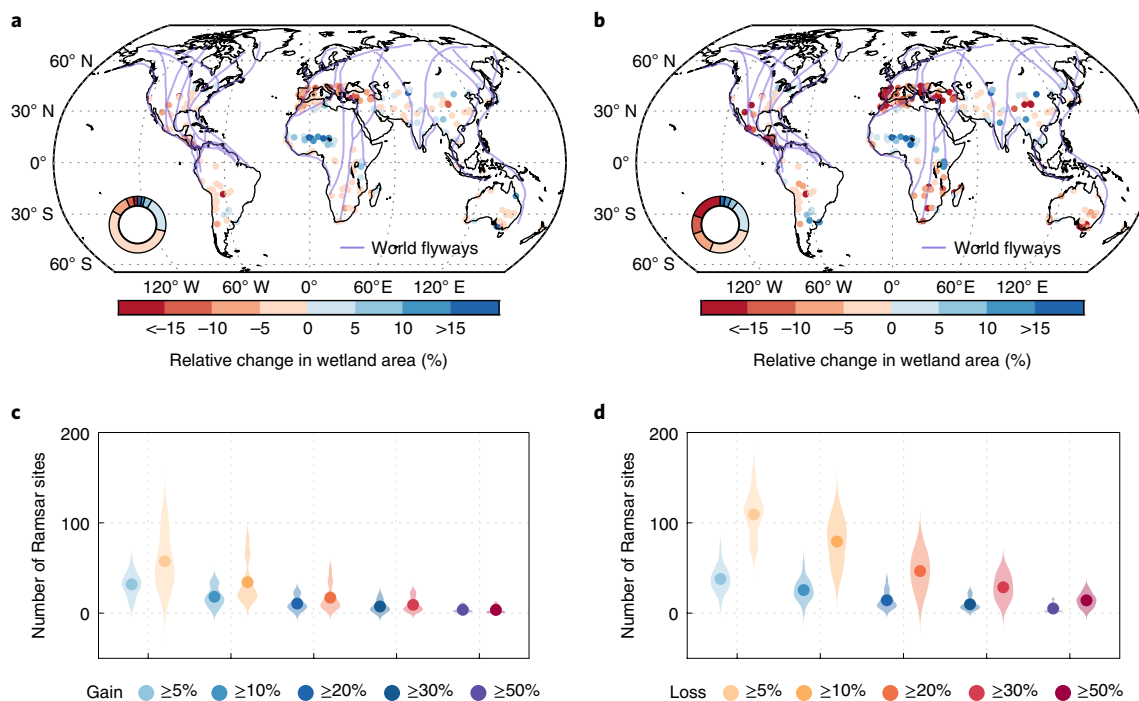


Fig. 5 | Wetland loss and waterbird migration. **a, b**, Projected change in wetland area in winter (December–February) for 2081–2100 relative to the reference period 1981–2000 under RCP 2.6 (13 models) (**a**) and RCP 8.5 (19 models) (**b**) from the CMIP5 ensemble across sites related to waterbirds (327 sites for C5 and C6). Only sites located south of 45°N are displayed given that most wetlands in high latitudes are frozen in winter. The lavender lines indicate global main migratory flyways⁴⁰. **c, d**, The distribution of the projected number of these sites related to waterbirds with at least 5%, 10%, 20%, 30% and 50% wetland gain or loss by the end of this century under RCP 2.6 (**c**) and RCP 8.5 (**d**). The wider parts of distributions signify that relatively more models project that number of sites will change.

8.5 during this century versus less than 70% under RCP 2.6, except in Latin America, where N_{-10} increases by 172% even for RCP 2.6 (Extended Data Fig. 6). By the end of this century, except in Asia, N_{-10} exceeds N_{+10} in all continents for the four RCP scenarios. Under RCP 8.5, Africa will have the largest positive imbalance between N_{-10} and N_{+10} (35 sites, IQR 41 sites), followed by Europe (32 sites, IQR 50 sites), and these two continents together contribute 68% (IQR 19%) of the increase of N_{-10} during this century. Note that roughly half of the global inland Ramsar sites are distributed in Europe, but these sites have on average a smaller area than those in Africa and Latin America, where most sites cover an area of more than 1,000 km² (Fig. 1a). The smaller number of Ramsar sites exposed to wetland loss in Africa and Latin America masks, however, the fact that those tropical Ramsar wetlands altogether will lose an area of 34,000 km² (IQR 51,000 km²) (~70% of global wetland-area loss) under RCP 8.5, versus only 4,000 km² (IQR 5,000 km²) for European sites (~10% of global wetland-area loss; Fig. 4 and Supplementary Table 3). According to the species–area relationship^{38,39}, the risks for wetland-dependent birds, fish and other animal and plant species thus would be more acute in Africa and Latin America. If limiting global warming to 1.5°C instead of 2°C, the projected N_{-10} will be reduced by 15% in these two tropical continents having key large wetland areas (Extended Data Fig. 6).

Implications for biodiversity

Given the distinct and complex implications of wetland-area loss on different ecosystem services, we map the risk of wetland loss by the end of this century across different criteria for Ramsar site designation for each continent (Extended Data Fig. 7). The risk of wetland loss for each criterion here is defined as the ratio of sites in the category N_{-10} for this criterion to all sites meeting this criterion. The risk of wetland loss will double between RCP 2.6

and RCP 8.5 across nearly all criteria in all continents. Under RCP 8.5, the risk of wetland loss in the two tropical continents with large wetland areas (Africa and Latin America) will be higher (~23%) for nearly all criteria. This indicates the projected large wetland-area losses in Africa and Latin America are controlled not only by the large site area, but also by the large fraction of shrinking sites. Under RCP 8.5, Africa and North America will face a higher risk of wetland loss for C5 and C6 categories (related to waterbirds), while sites in Europe and Latin America will face a higher risk of wetland loss for C7 (related to indigenous fishes) and C8 (related to migratory fishes) categories. The higher risk of wetland loss for sites meeting C5, C7 and C8 suggests that wetland losses induced by global warming threaten not only local species, but also migrating species.

To clearly show the potential risk of wetland loss on waterbird migration and survival, we intersect the world main flyways of migratory birds⁴⁰ with our map of change in wetland area across sites located south of 45°N in winter (December–January) (Fig. 5). Sites that are important to waterbirds are predicted to face a larger risk of area loss (a net wetland loss of 3,000 km²) by 2100 under RCP 8.5, with an area loss of larger than 10% in 29% of sites (IQR 20%), compared with 23% (IQR 9%) for all inland Ramsar sites. As important migratory corridors and foraging hotspots, projected large-scale and simultaneous wetland loss in sites located in the Mediterranean, Mexico and Central America, and South Africa under RCP 8.5 will lead to a substantial deterioration of American and African–Eurasian flyways. Migratory waterbirds on these flyways could have difficulty finding substitute stop-off points during the migration from the Northern Hemisphere. Increased exposure to habitat loss and food shortage could further aggravate the risk of population loss during long-distance migration for vulnerable waterbird species.

Conclusions

Our analyses suggest that the risk of wetland loss for global inland Ramsar sites will increase with the warming level of future climate. By the end of this century, despite a modest global gross (<5%, 21,000–46,000 km²) and net (~1%, 6,000–10,000 km²) loss of inland Ramsar wetlands under four warming scenarios, the effects of climate change on Ramsar wetlands are projected to be pronounced at regional scales. Sites with a much higher loss percentage than the global average dominate in Mediterranean, Mexico and Central America, central Latin America and South Africa—all part of a global biodiversity hotspot network. The consensus prediction of wetland loss in these regions by CMIP5 climate models suggests biodiversity threats due to habitat loss. Compared with global inland wetlands, percentage changes in wetland area across all inland Ramsar sites is estimated to be close to the global baseline (Fig. 3 and Extended Data Fig. 8), but noticeable disagreements found in each continent point out Ramsar sites underrepresentative of broader wetlands at the continent scale.

Limited by the uncertainties in the observed wetland map for parameter calibration and a series of simplifying assumptions established in TOPMODEL (Methods and Supplementary Discussion 2), some small wetlands, including peatlands, floodplains and thermokarst lakes, may be missed in our model. In addition, keeping the lake area within Ramsar sites constant could propagate biases in the projection of future wetland area, in particular for those sites located in high latitudes, which could be experiencing an expanded lake area due to global climate warming. Although the parameter calibration with the observation-based wetland map and a small proportion of lake area in the total area of global inland Ramsar sites ensure the reliability of our projection, incorporating floodplain models and process-based thermokarst lake models could further improve the projection of global wetland dynamics^{41–43}. The dynamics of global lakes not accounted for here need further investigation.

Compared with the high warming level under RCP 8.5, climate mitigation to stabilize global climate change at 1.5 °C and 2 °C could save 123 and 105 sites, respectively, from a wetland loss larger than 10%. The net wetland loss could be reduced by 40% (4,000 km²) from RCP 8.5 to RCP 2.6, in particular much less loss in biodiversity hotspot regions such as the Mediterranean, central Latin America and South Africa. Thus, to lower the risk of wetland losses and to facilitate biodiversity conservation on wetland hotspot sites, climate mitigation is indispensable and should be carried out immediately due to higher risk with later mitigation⁴⁴. The risk of wetland loss in migration flyways projected under further global warming highlights that all wetlands along migration flyways should be considered as a whole by international collaboration and coordinated action.

Online content

Any methods, additional references, Nature Research reporting summaries, source data, extended data, supplementary information, acknowledgements, peer review information; details of author contributions and competing interests; and statements of data and code availability are available at <https://doi.org/10.1038/s41558-020-00942-2>.

Received: 24 August 2019; Accepted: 29 September 2020;

Published online: 02 November 2020

References

- Creed, I. F. et al. Enhancing protection for vulnerable waters. *Nat. Geosci.* **10**, 809–815 (2017).
- Davidson, N. C. How much wetland has the world lost? Long-term and recent trends in global wetland area. *Mar. Freshw. Res.* **65**, 934–941 (2014).
- Gong, P. et al. China's wetland change (1990–2000) determined by remote sensing. *Sci. China Earth Sci.* **53**, 1036–1042 (2010).
- Zedler, J. B. & Kercher, S. Wetland resources: status, trends, ecosystem services, and restorability. *Annu. Rev. Env. Resour.* **30**, 39–74 (2005).
- Finlayson, M. et al. *Millennium Ecosystem Assessment: Ecosystems and Human Well-Being: Wetlands and Water Synthesis* (Island Press, 2005).
- Keddy, P. A. et al. Wet and wonderful: the world's largest wetlands are conservation priorities. *Bioscience* **59**, 39–51 (2009).
- Global Wetland Outlook: State of the World's Wetlands and Their Services to People* (Ramsar Convention Secretariat, 2018).
- Russi, D. et al. *The Economics of Ecosystems and Biodiversity for Water and Wetlands* (Ramsar Secretariat, 2013).
- Moomaw, W. R. et al. Wetlands in a changing climate: science, policy and management. *Wetlands* **38**, 183–205 (2018).
- Tootchi, A., Jost, A. & Ducharme, A. Multi-source global wetland maps combining surface water imagery and groundwater constraints. *Earth Syst. Sci. Data* **11**, 189–220 (2019).
- Davidson, N. C., Fluet-Chouinard, E. & Finlayson, C. M. Global extent and distribution of wetlands: trends and issues. *Mar. Freshw. Res.* **69**, 620–627 (2018).
- Dixon, M. J. R. et al. Tracking global change in ecosystem area: the wetland extent trends index. *Biol. Conserv.* **193**, 27–35 (2016).
- Sievers, M., Hale, R., Parris, K. M. & Swearer, S. E. Impacts of human-induced environmental change in wetlands on aquatic animals. *Biol. Rev.* **93**, 529–554 (2018).
- Prigent, C. et al. Changes in land surface water dynamics since the 1990s and relation to population pressure. *Geophys. Res. Lett.* **39**, L08403 (2012).
- Schroeder, R. et al. Development and evaluation of a multi-year fractional surface water data set derived from active/passive microwave remote sensing data. *Remote Sens.* **7**, 16688–16732 (2015).
- Čížková, H. et al. Actual state of European wetlands and their possible future in the context of global climate change. *Aquat. Sci.* **75**, 3–26 (2013).
- Reis, V. et al. A global assessment of inland wetland conservation status. *Bioscience* **67**, 523–533 (2017).
- Vörösmarty, C. J. et al. Global threats to human water security and river biodiversity. *Nature* **467**, 555–561 (2010).
- Comyn-Platt, E. et al. Carbon budgets for 1.5 and 2 °C targets lowered by natural wetland and permafrost feedbacks. *Nat. Geosci.* **11**, 568–573 (2018).
- Gedney, N., Cox, P. M. & Huntingford, C. Climate feedback from wetland methane emissions. *Geophys. Res. Lett.* <https://doi.org/10.1029/2004gl020919> (2004).
- Zhang, Z. et al. Emerging role of wetland methane emissions in driving 21st century climate change. *Proc. Natl Acad. Sci. USA* **114**, 9647–9652 (2017).
- Dai, A. Increasing drought under global warming in observations and models. *Nat. Clim. Change* **3**, 52–58 (2013).
- IPCC *Climate Change 2013: The Physical Science Basis* (eds Stocker, T. F. et al.) (Cambridge Univ. Press, 2013).
- Yang, H. et al. Regional patterns of future runoff changes from Earth system models constrained by observation. *Geophys. Res. Lett.* **44**, 5540–5549 (2017).
- Even, K. J. & Kirkby, M. J. A physically based, variable contributing area model of basin hydrology / Un modèle à base physique de zone d'appel variable de l'hydrologie du bassin versant. *Hydrol. Sci. Bull.* **24**, 43–69 (1979).
- Stocker, B. D., Spahni, R. & Joos, F. DYPTOP: a cost-efficient TOPMODEL implementation to simulate sub-grid spatio-temporal dynamics of global wetlands and peatlands. *Geosci. Model Dev.* **7**, 3089–3110 (2014).
- Decharme, B. & Douville, H. Introduction of a sub-grid hydrology in the ISBA land surface model. *Clim. Dynam.* **26**, 65–78 (2006).
- Habets, F. & Saulnier, G. M. Subgrid runoff parameterization. *Phys. Chem. Earth Part B* **26**, 455–459 (2001).
- Ringeval, B. et al. Modelling sub-grid wetland in the ORCHIDEE global land surface model: evaluation against river discharges and remotely sensed data. *Geosci. Model Dev.* **5**, 941–962 (2012).
- Zhang, Z., Zimmermann, N. E., Kaplan, J. O. & Poulter, B. Modeling spatiotemporal dynamics of global wetlands: comprehensive evaluation of a new sub-grid TOPMODEL parameterization and uncertainties. *Biogeosciences* **13**, 1387–1408 (2016).
- Rodell, M. et al. The global land data assimilation system. *Bull. Am. Meteorol. Soc.* **85**, 381–394 (2004).
- Taylor, K. E., Stouffer, R. J. & Meehl, G. A. An overview of CMIP5 and the experiment design. *Bull. Am. Meteorol. Soc.* **93**, 485–498 (2012).
- Mathews, T. R., Dadson, S. J., Lehner, B., Abele, S. & Gedney, N. High-resolution global topographic index values for use in large-scale hydrological modelling. *Hydrol. Earth Syst. Sci.* **19**, 91–104 (2015).
- Pekel, J. F., Cottam, A., Gorelick, N. & Belward, A. S. High-resolution mapping of global surface water and its long-term changes. *Nature* **540**, 418–422 (2016).
- Beck, H. E. et al. MSWEP: 3-hourly 0.25° global gridded precipitation (1979–2015) by merging gauge, satellite, and reanalysis data. *Hydrol. Earth Syst. Sci.* **21**, 589–615 (2017).

36. Martens, B. et al. GLEAM v3: satellite-based land evaporation and root-zone soil moisture. *Geosci. Model Dev.* **10**, 1903–1925 (2017).
37. Niu, G., Yang, Z., Dickinson, R. E. & Gulden, L. E. A simple TOPMODEL-based runoff parameterization (SIMTOP) for use in global climate models. *J. Geophys. Res.* **110**, D21106 (2005).
38. Lomolino, M. V. Ecology's most general, yet protean pattern: the species–area relationship. *J. Biogeogr.* **27**, 17–26 (2000).
39. Powers, R. P. & Jetz, W. Global habitat loss and extinction risk of terrestrial vertebrates under future land-use-change scenarios. *Nat. Clim. Change* **9**, 323–329 (2019).
40. New study highlights gaps in protection for migratory birds globally. *CMS* <https://www.cms.int/en/news/new-study-highlights-gaps-protection-migratory-birds-globally> (2015).
41. Lu, X., Zhuang, Q., Liu, Y., Zhou, Y. & Aghakouchak, A. A large-scale methane model by incorporating the surface water transport. *J. Geophys. Res. Biogeosci.* **121**, 1657–1674 (2016).
42. Tan, Z. & Zhuang, Q. Methane emissions from pan-Arctic lakes during the 21st century: an analysis with process-based models of lake evolution and biogeochemistry. *J. Geophys. Res. Biogeosci.* **120**, 2641–2653 (2015).
43. Schuur, E. A. G. et al. Climate Change and the permafrost carbon feedback. *Nature* **520**, 171–179 (2015).
44. Warren, R. et al. Quantifying the benefit of early climate change mitigation in avoiding biodiversity loss. *Nat. Clim. Change* **3**, 678–682 (2013).

Publisher's note Springer Nature remains neutral with regard to jurisdictional claims in published maps and institutional affiliations.

© The Author(s), under exclusive licence to Springer Nature Limited 2020

Methods

Global climatic datasets. The monthly total SM and soil temperature (ST) data to calculate historical water table for the period 1980–2014 are obtained from GLDAS-Noah v.2.0, which is a reanalysis product jointly developed by National Aeronautics and Space Administration (NASA) Goddard Space Flight Center (GSFC) and the National Oceanic and Atmospheric Administration (NOAA) National Centers for Environmental Prediction (NCEP)⁵¹. With a spatial resolution of $0.25^\circ \times 0.25^\circ$, GLDAS-Noah v.2.0 assimilates satellite- and ground-based observations to produce optimal fields of land surface states and fluxes in near-real time. The SM estimation from GLDAS-Noah v.2.0 agrees well with a wealth of ground-based in situ observations and independent remote-sensing products^{45,46}. The SM and ST in the land surface model are provided at four vertical layers (0–0.1, 0.1–0.4, 0.4–1 and 1–2 m). In addition, we use SM data from GLEAM v.3.2a (ref.³⁶) to investigate the change in SM for the period 1980–2014. With a spatial resolution of $0.25^\circ \times 0.25^\circ$, GLEAM SM data assimilate the surface SM from satellite microwave observations into the soil profile as well as other observed climate variables in the water-bucket model. It provides the estimation of SM at the surface and in the root zone; the depth of surface SM is 0.1 m while the root-zone depth is not uniform globally and depends on local conditions, with a range of 0.1–2.5 m.

The global gridded monthly air temperature data used in this study are the Climatic Research Unit TS v.4.01 dataset for the period 1980–2014, with a spatial resolution of $0.5^\circ \times 0.5^\circ$. The monthly ET from 1980 to 2014 is obtained from GLEAM v.3.2a (ref.³⁶). We use the monthly P (precipitation) data from Multi-Source Weighted-Ensemble Precipitation v.2.1 precipitation product³⁵ with a spatial resolution of $0.1^\circ \times 0.1^\circ$ for the period 1980–2014, the same P used in GLEAM v.3.2a. To reduce the effects of errors in fine-scale spatial structure on estimation of climate change in Ramsar sites over the past decades, all these data sets are regridded into $0.5^\circ \times 0.5^\circ$.

CMIP5 climate model data. The historical simulations (analysed years 1980–2005) and four scenario-dependent projections (RCP 2.6, RCP 4.5, RCP 6.0 and RCP 8.5; analysed years 2006–2100) of monthly T, P, surface SM, total SM, ET, runoff (R), and ST are obtained from the CMIP5 archive³⁷. All model outputs for the period 1980–2100 are regridded to the resolution of $0.5^\circ \times 0.5^\circ$ using the first-order conservative remapping technique³⁸. Models that provide monthly SM and ST in each soil layer of both historical simulations and future projections for the calculation of water table depth (WTD) are selected for the projections (Supplementary Table 2 and Supplementary Discussion 1). Because there are considerable uncertainties in SM estimation in CMIP5 climate models, we correct the historical and future SM and ST output from CMIP5 models at grid scale by a correction factor: the ratio of mean annual SM from 1980 to 2005 from GLDAS-Noah v.2.0 to that from CMIP5 models.

Ramsar site data. The general information (including location, area, wetland type, ecosystem services and so on) of 1,352 inland Ramsar sites is obtained from the Ramsar Sites Information Service (<https://rsis.ramsar.org/>). The coastal and human-made Ramsar sites are not considered in this study because these wetland types cannot be simulated by TOPMODEL. The shapefile data of vector boundaries of the sites are collected from the Ramsar Sites Information Service and the World Database on Protected Areas⁴⁹. Note that there are only 926 sites with available shapefile data. For those sites without shapefile data, we treat each as a regular square associated with its location, and the size of the regular square is determined by its area. Then the climate variables for a Ramsar site are calculated as wetland-area-weighted average of all grids within the polygon of this site. For the extraction of wetland area, a buffer for each Ramsar site is created given that wetland gain or loss may be found outside of the site boundary for future wetland change projections. The area of the buffer is four times the size of the site.

Global wetland maps. We use the RFW map¹⁰ to calibrate parameters of the TOPMODEL-based diagnostic model. RFW is a set of high-resolution maps (15 arcsec) of regularly flooded wetlands, developed by overlapping three open-water and inundation datasets derived from satellite imagery: the European Space Agency Climate Change Initiative land cover⁵⁰, Global Inundation Extent from Multi-Satellites (GIEMS-D15) inundation surface⁵¹ and the maximum water extent from the Joint Research Centre (JRC) surface water dataset⁵⁴. Because TOPMODEL cannot simulate artificial rice paddies, we remove maximum irrigated and rain-fed rice agriculture from the RFW using the global dataset of Monthly Irrigated and Rainfed Crop Areas (MIRCA2000)⁵². In this study, we consider the RFW map as the long-term maximum wetland area. Overall, the RFW map covers 8.2% of the land surface area (10.9 million km²), including open flooded wetlands and inundation area under canopy but excluding lakes and rice paddies (Supplementary Fig. 9e).

We also use a detailed static pantropical (40° N to 60° S) wetland map from Gumbrecht et al.⁵³ (hereafter named G2017) including both peatlands and floodplains to calibrate the parameters of the TOPMODEL-based diagnostic model, for the uncertainty of wetland maps (Supplementary Table 4 and Supplementary Figs. 9 and 10). The G2017 wetland map, derived from a hybrid expert system, identifies not only permanently and seasonally wetland areas, but also soil wetness and topographic conditions that favour waterlogging in the

absence of flooding (due to rain-fed or groundwater-fed sources). To verify our simulations of wetlands area on peatlands and floodplains, two global peatland maps^{54,55} and one regional floodplain map in the Amazon⁵⁶ are used here (Supplementary Discussion 2 and Supplementary Figs. 9 and 10).

The TOPMODEL-based diagnostic model. To simulate global wetland dynamics, we use a TOPMODEL-based diagnostic model from Stocker et al.²⁶ that has successfully predicted the spatial distribution, extent and seasonality of natural wetlands. The procedures for the parameter calibration of the diagnostic model and the projection of future wetland dynamics are shown in Extended Data Fig. 2.

Following the classical TOPMODEL framework, an analytical relationship between the water table and the local topographic index distributions in a catchment is given under the assumptions that the local hydraulic gradient is approximated by the local topographic slope and the water-table variations can be assimilated to a succession of steady states with uniform recharge²⁵. At grid scale, the analytical relationship can be represented as:

$$CTI_i - \overline{CTI}_x = -M(\Gamma_i - \overline{\Gamma}_x) \quad (1)$$

where CTI indicates compound topographic index, defined as the log of the ratio of contributing area to local slope. The CTI data used in this study are from Marthews et al.³³ with the spatial resolution of $500 \text{ m} \times 500 \text{ m}$, where lakes and reservoirs are removed with Global Lakes and Wetlands Data (Lehner and Döll⁵⁷). The index x and index i indicate the grid and the sub-grid (hereafter called the pixel), respectively. CTI_i indicates the CTI of the pixel i while \overline{CTI}_x is the mean CTI of the grid cell x . Similarly, Γ_i is the WTD of the pixel i and $\overline{\Gamma}_x$ is the mean WTD of the grid cell x . M is a tunable parameter that describes the exponential decrease of soil transmissivity with depth²⁵. When the water table of the pixel i is at the soil surface (that is, $\Gamma_i = 0$), the CTI threshold to be flooded for the grid x is derived:

$$CTI_x^* = \overline{CTI}_x + M \times \overline{\Gamma}_x \quad (2)$$

Then the percentage of pixels with CTI_i larger than the thresholds CTI_x^* is considered as the inundated fraction in the grid x (f_x):

$$f_x = \frac{1}{A_x} \sum_i A_i^*, \text{ with } A_i^* = \begin{cases} A_i & \text{if } CTI_i \geq CTI_x^* \\ 0 & \text{if } CTI_i < CTI_x^* \end{cases} \quad (3)$$

In this study, the wetlands are defined as inundated/saturated area simulated by the diagnostic model. The annual maximum of monthly inundation area is used in analyses of Figs. 2–4. Winter average inundation area south of 45° N is used in the analysis of Fig. 5.

Although the TOPMODEL can address the simulation of global wetland extent by downscaling the water-table depth with the relatively higher-resolution CTI data as described in the preceding, the computational cost would be large when employed to produce the long time-series wetland dynamics. To solve this problem, we apply an asymmetric sigmoid function Ψ proposed by Stocker et al.²⁶ to fit the relationship between f_x and $\overline{\Gamma}_x$ from TOPMODEL directly at $0.5^\circ \times 0.5^\circ$ resolution:

$$\Psi(\overline{\Gamma}_x) = \left(1 + v_x \times e^{-k_x(\overline{\Gamma}_x - q_x)} \right)^{-1/v_x} \quad (4)$$

where v_x , k_x , q_x are three parameters. According to the TOPMODEL framework, with the CTI distribution for a grid, the choice of the parameter M determines the relationship between f_x and $\overline{\Gamma}_x$ (Equations (2) and (3)) and then determines the values of v_x , k_x , and q_x in Equation (4). Given the distinct topography, soil types and other intrinsic characteristics in different regions, we consider M as a tunable, globally heterogeneous and grid-specific parameter, with a range of 1–15. With a sequence of assumed $\overline{\Gamma}_x$ spanning a plausible range of values (–1 m to 2 m) and corresponding f_x from the TOPMODEL, a range of 1–15 for M means there are 15 sets of (v_x , k_x , q_x) for each $0.5^\circ \times 0.5^\circ$ grid following the framework of Stocker et al.²⁶. The optimized parameter combination of (v_x , k_x , q_x) is determined by selecting the minimum root mean square error (RMSE, defined in Equation (5)) of long-term maximum wetland extent between simulations and observation from RFW, among 15 simulations determined by the parameter M :

$$RMSE = \sqrt{\frac{\sum_{i=1}^n (O_i - P_i)^2}{n}} \quad (5)$$

where O_i and P_i are the observed and simulated wetland extent, respectively. As shown in Extended Data Fig. 3, our simulation can reproduce the spatial pattern of global wetland fraction from RFW in most regions with an RMSE less than 3% but underestimates the wetland extent in the south of the Hudson Bay, northern Siberia and India. Because only a few inland Ramsar sites are located in these regions (Fig. 1), this would have little effect on our results. More than 75% of sites have an RMSE less than 3%.

The extraction of wetland area for global inland Ramsar sites. With the optimized parameters (v_x , k_x and q_x) and monthly WTD from GLDAS-Noah v.2.0 and CMIP5 climate models, the global wetland dynamics are produced for

the period 1980–2100 at 0.5°×0.5° resolution⁵⁸. Given that not all areas within a Ramsar site are inundation areas, we use the CTI distribution at 500 m×500 m resolution to identify the flooded pixels within a grid (Extended Data Fig. 9) according to the simulated wetland fraction of this grid, and then calculate the wetland area for each site by aggregating all flooded pixels within the buffer of the site⁵⁸. Note that change in wetland area in 102 sites located in islands and coastal regions cannot be projected because SM data from CMIP5 models and/or RFW data are not available there. Thus, only 1,250 sites out of the 1,352 inland Ramsar sites are presented here. In Extended Data Fig. 9, we show an example of wetland change extraction in a Ramsar site, Shengjin Lake National Nature Reserve, by the end of this century under RCP 2.6 and RCP 8.5. In addition, we extract the change in surface open water for each Ramsar site from 1984 to 2015 as independent satellite-based evidence for the sign of historical change in wetland area, by intersecting shapefiles of Ramsar sites and the transition map of JRC global surface water products⁵⁴ with 30 m×30 m resolution (Supplementary Fig. 1a).

Data availability

The shapefile data of the Ramsar inland sites are available from the Ramsar Sites Information Service (<https://rsis.ramsar.org/>) and the World Database on Protected Areas (<http://datasets.wri.org/dataset/64b69c0fb0834351bd6c0ceb3744c5ad>). The global gridded topographic index data are available from <https://doi.org/10.5285/6b0c4358-2bf3-4924-aa8f-793d468b92be>. The CRU TS v.4.01 climate datasets are available from CRU (https://crudata.uea.ac.uk/cru/data/hrg/cru_ts_4.01/). The GLEAM v.3.2a data sets are available at <https://www.gleam.eu/>. The MSWEP v.2.1 datasets are available at <http://www.gloh2o.org/>. The JRC surface water products are available at <https://global-surface-water.appspot.com/download>. The RFW datasets are available from <https://doi.pangaea.de/10.1594/PANGAEA.892657>. The GLDAS-Noah v.2.0 datasets are available at https://disc.gsfc.nasa.gov/datasets/GLDAS_NOAH025_M_V2.0/summary?keywords=GLDAS. All CMIP5 data can be accessed from the CMIP5 archive (<https://esgf-node.llnl.gov/search/cmip5/>). The change in wetland area in different projected epochs for each Ramsar site under the four RCP scenarios is publicly available on GitHub (https://github.com/yixixy/Ramsar_wetlands_change)⁵⁸. Source data are provided with this paper.

Code availability

Computer codes to simulate wetland area by TOPMODEL and to analyse the change in wetland area for Ramsar sites are publicly available on GitHub (https://github.com/yixixy/Ramsar_wetlands_change)⁵⁸.

References

45. Wang, A. & Zeng, X. Evaluation of multireanalysis products with in situ observations over the Tibetan Plateau. *J. Geophys. Res. Atmos.* **117**, D05102 (2012).
46. Bi, H., Ma, J., Zheng, W. & Zeng, J. Comparison of soil moisture in GLDAS model simulations and in situ observations over the Tibetan Plateau. *J. Geophys. Res. Atmos.* **121**, 2658–2678 (2016).
47. *Model Output from the Coupled Model Intercomparison Project Phase 5* (WCRP, accessed 12 July 2018); <https://esgf-node.llnl.gov/search/cmip5/>
48. Jones, P. W. First- and second-order conservative remapping schemes for grids in spherical coordinates. *Mon. Weather Rev.* **127**, 2204–2210 (1999).
49. *Protected Planet: The World Database on Protected Areas* (UNEP-WCMC and IUCN, accessed 12 July 2018); <https://datasets.wri.org/dataset/64b69c0fb0834351bd6c0ceb3744c5ad>
50. Herold, M., Van Groenestijn, A., Kooistra, L., Kalogirou, V. & Arino, O. *Land Cover CCI, Product User Guide Version 2.0* (ESA, 2015); https://maps.elie.ucl.ac.be/CCI/viewer/download/ESACCI-LC-Ph2-PUGv2_2.0.pdf
51. Fluet-Chouinard, E., Lehner, B., Rebelo, L.-M., Papa, F. & Hamilton, S. K. Development of a global inundation map at high spatial resolution from topographic downscaling of coarse-scale remote sensing data. *Remote Sens. Environ.* **158**, 348–361 (2015).
52. Portmann, F. T., Siebert, S. & Döll, P. MIRCA2000—global monthly irrigated and rainfed crop areas around the year 2000: a new high-resolution data set for agricultural and hydrological modeling. *Glob. Biogeochem. Cycles* **24**, GB1011 (2010).
53. Gumbrecht, T. et al. An expert system model for mapping tropical wetlands and peatlands reveals South America as the largest contributor. *Glob. Change Biol.* **23**, 3581–3599 (2017).
54. Xu, J., Morris, P., Liu, J. & Holden, J. PEATMAP: refining estimates of global peatland distribution based on a meta-analysis. *Catena* **160**, 134–140 (2018).
55. Yu, Z., Loisel, J., Brosseau, D. P., Beilman, D. W. & Hunt, S. J. Global peatland dynamics since the Last Glacial Maximum. *Geophys. Res. Lett.* **37**, L13402 (2010).
56. Lauerwald, R. et al. ORCHILEAK (revision 3875): a new model branch to simulate carbon transfers along the terrestrial–aquatic continuum of the Amazon basin. *Geosci. Model Dev.* **10**, 3821–3859 (2017).
57. Lehner, B. & Döll, P. Development and validation of a global database of lakes, reservoirs and wetlands. *J. Hydrol.* **296**, 1–22 (2004).
58. Xi, Y., Peng, S., Ciais, P. & Chen, Y. Code and data for simulating future impacts of climate change on inland Ramsar wetlands (Version v1.0.0). *Zenodo* <https://doi.org/10.5281/zenodo.4018712> (2020).

Acknowledgements

This study was supported by the National Natural Science Foundation of China (grant numbers 41722101, 41830643 and 41671079). P.C. acknowledges support from the ERC Synergy grant ERC-2013-SyG-610028 IMBALANCE-P and the ANR CLAND convergence institute. Y.C. acknowledges support from the Second Tibetan Plateau Scientific Expedition and Research Program (2019QZKK0303).

Author contributions

S.P. conceived and designed the study. Y.X. performed the analysis and created all the figures. S.P., P.C. and Y.X. wrote the manuscript with contribution from Y.C.

Competing interests

The authors declare no competing interests.

Additional information

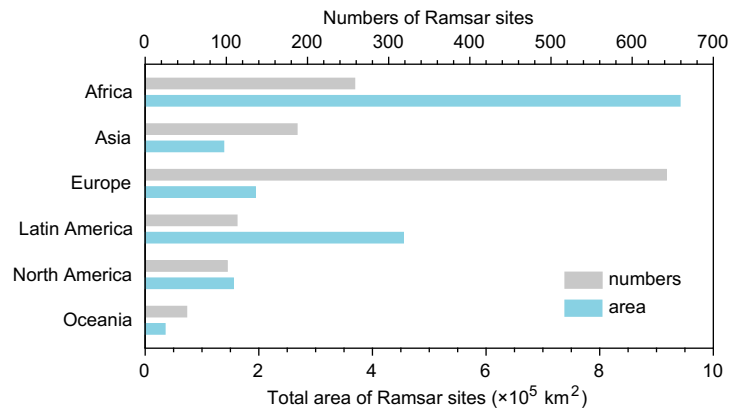
Extended data is available for this paper at <https://doi.org/10.1038/s41558-020-00942-2>.

Supplementary information is available for this paper at <https://doi.org/10.1038/s41558-020-00942-2>.

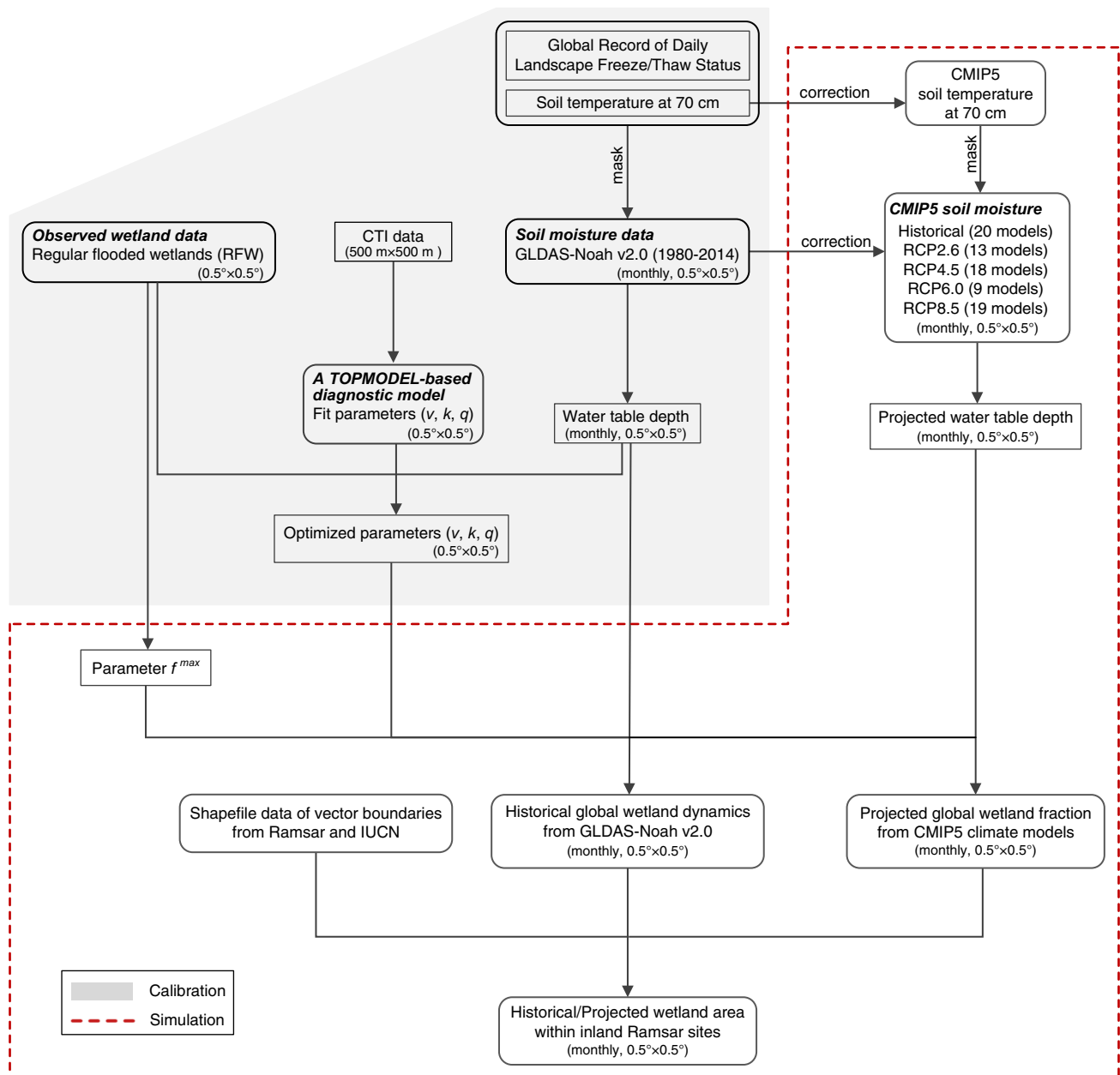
Correspondence and requests for materials should be addressed to S.P.

Peer review information *Nature Climate Change* thanks Etienne Fluet-Chouinard, Zhenguo Niu and the other, anonymous, reviewer(s) for their contribution to the peer review of this work.

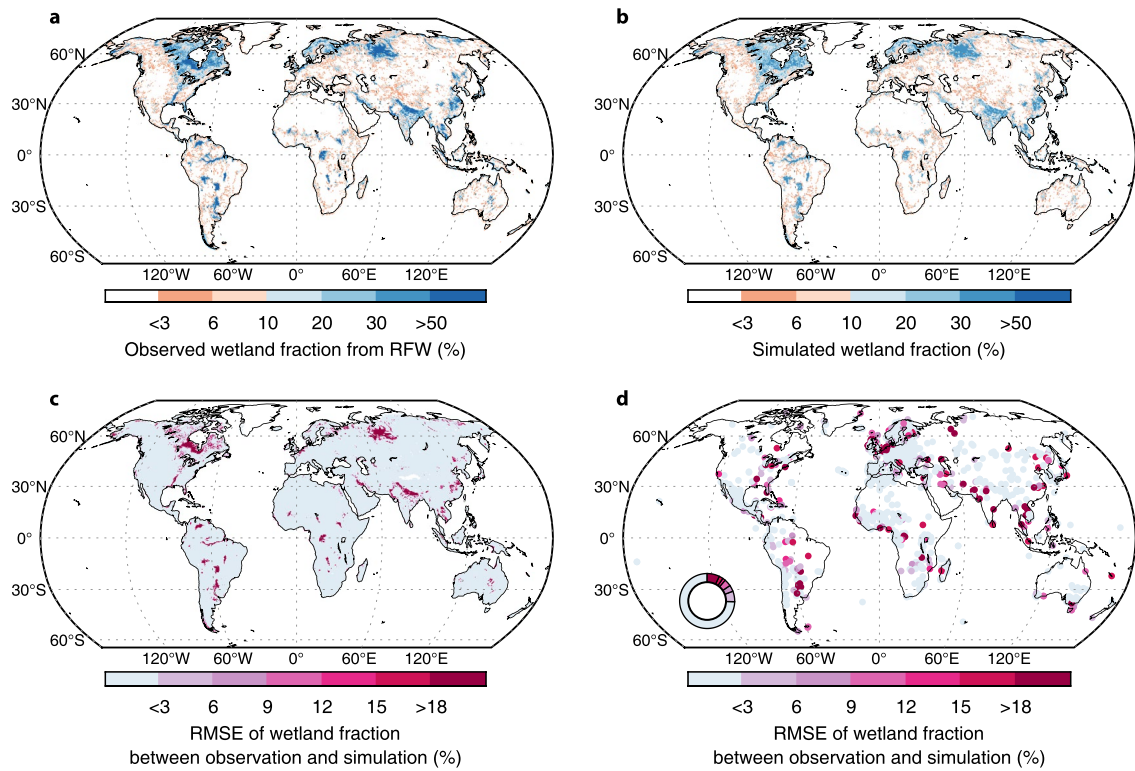
Reprints and permissions information is available at www.nature.com/reprints.



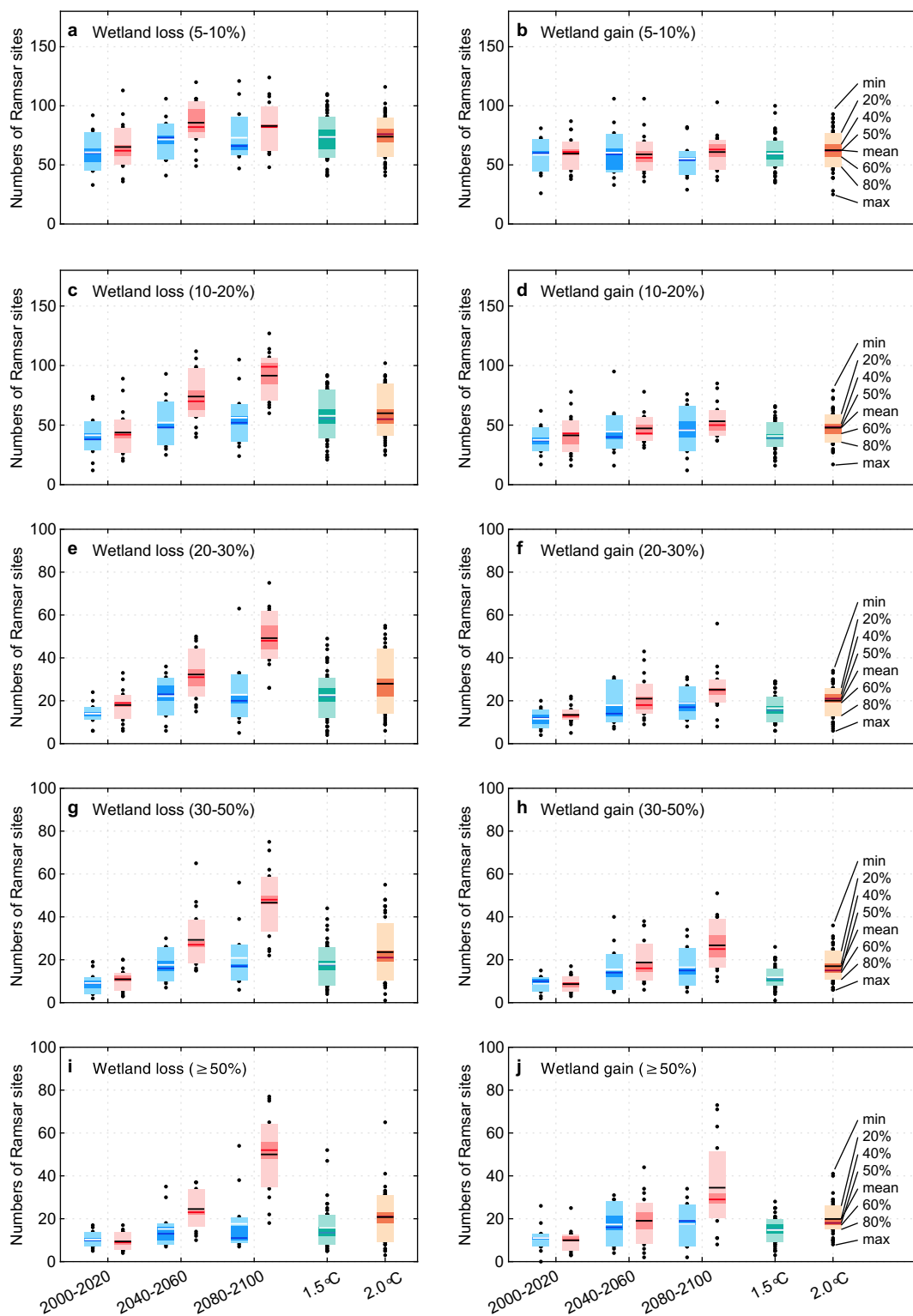
Extended Data Fig. 1 | Statistics of numbers and total area of inland Ramsar sites in six continents. Numbers and total area of inland Ramsar sites in six continents including Africa, Asia, Europe, Latin America, North America, and Oceania.



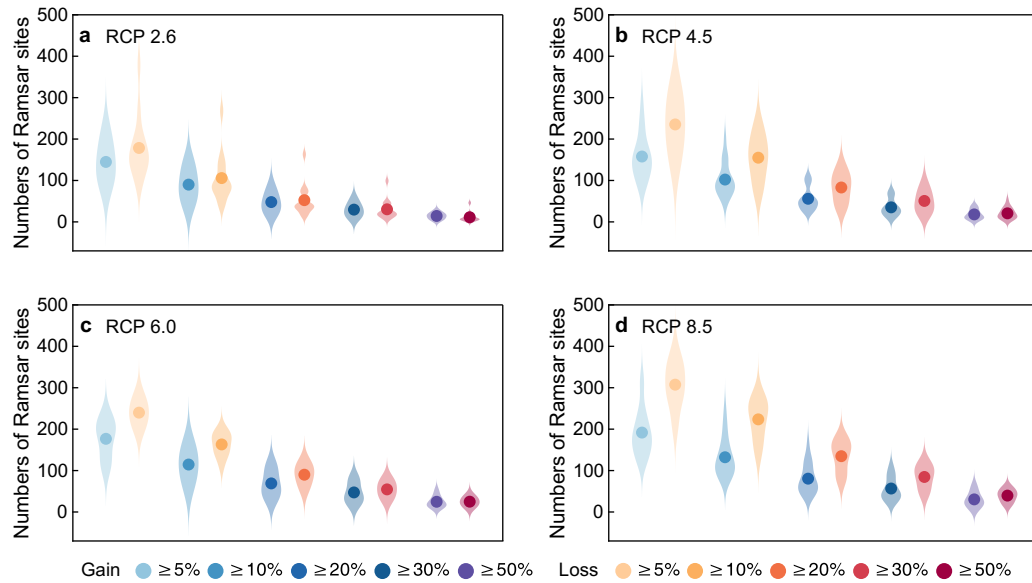
Extended Data Fig. 2 | Diagram of workflow for simulating wetland dynamics across global inland Ramsar sites. Workflow for simulating historical (1980–2014) and future (1980–2100) wetland dynamics based on soil moisture from GLDAS Noah v2.0 and CMIP5 climate models under four RCP scenarios.



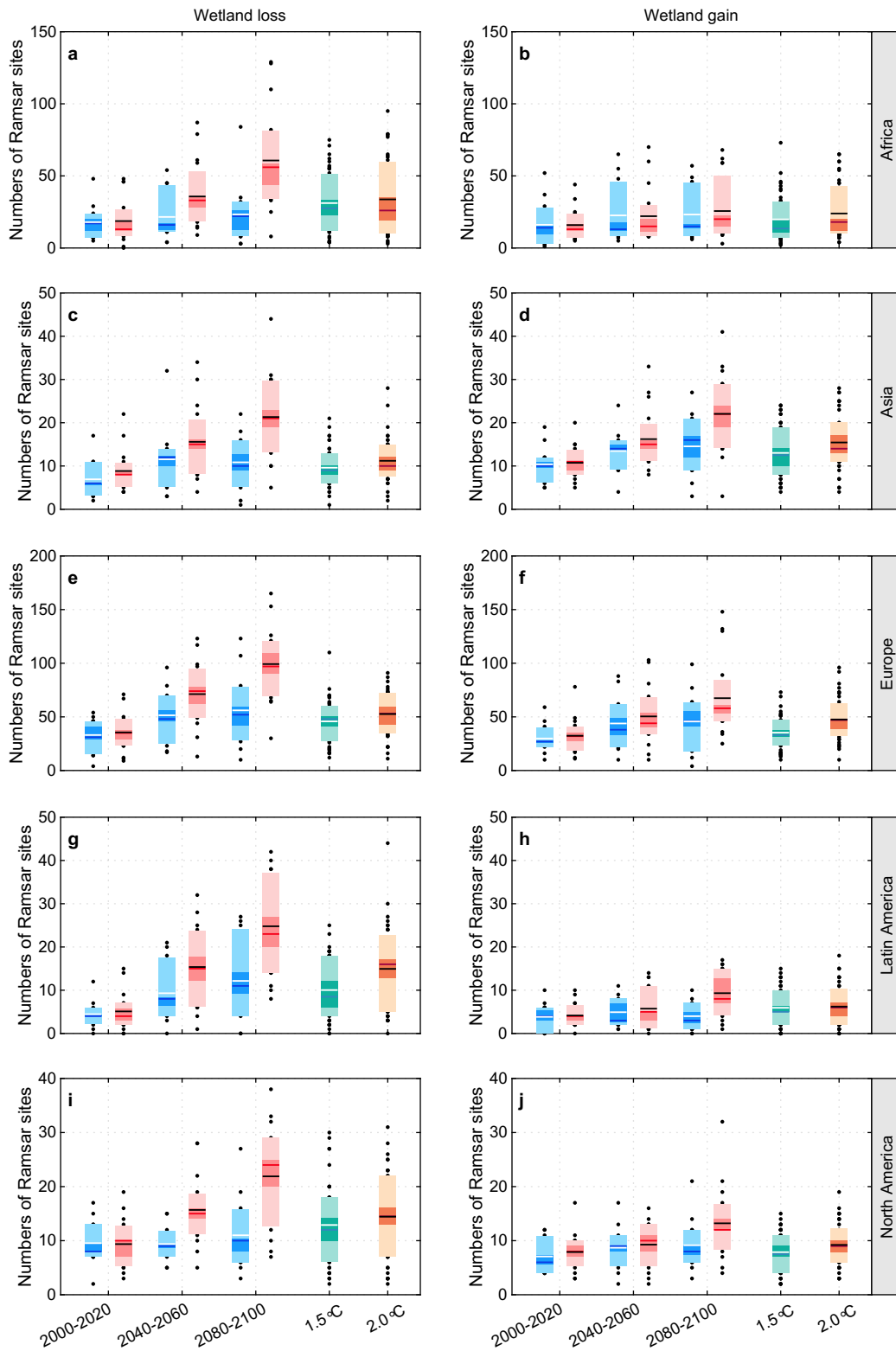
Extended Data Fig. 3 | Evaluation of the TOPMODEL-based hydrological model. Spatial patterns of long-term maximum wetland fraction from RFW (a) and historical simulation with GLDAS-Noah v2.0 (b), as well as RMSE (the minimum root-mean-square-error) between RFW and the simulation over global wetlands (c) and inland Ramsar sites (d).



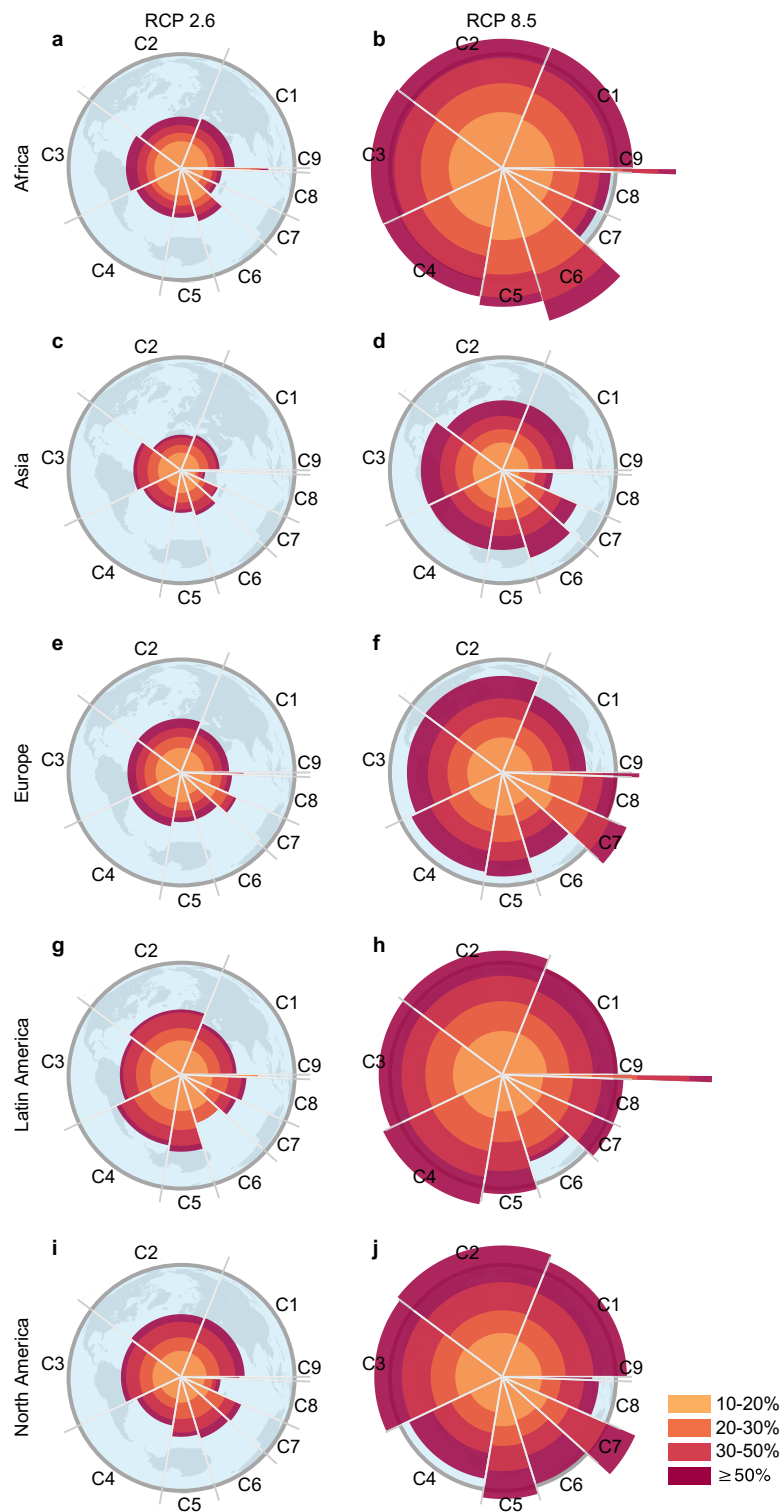
Extended Data Fig. 4 | Same as Fig. 2, but for temporal changes in numbers of global inland Ramsar sites with wetland loss/gain of five different cutoffs. **a, c, e, g, and i** show temporal changes in numbers of sites with wetland loss of 5-10%, 10-20%, 20-30%, 30-50%, and over 50% respectively through the 21st century under RCP2.6 and RCP8.5, while **b, d, f, h, and j** are for numbers of sites with wetland gain of 5-10%, 10-20%, 20-30%, 30-50%, and over 50% respectively.



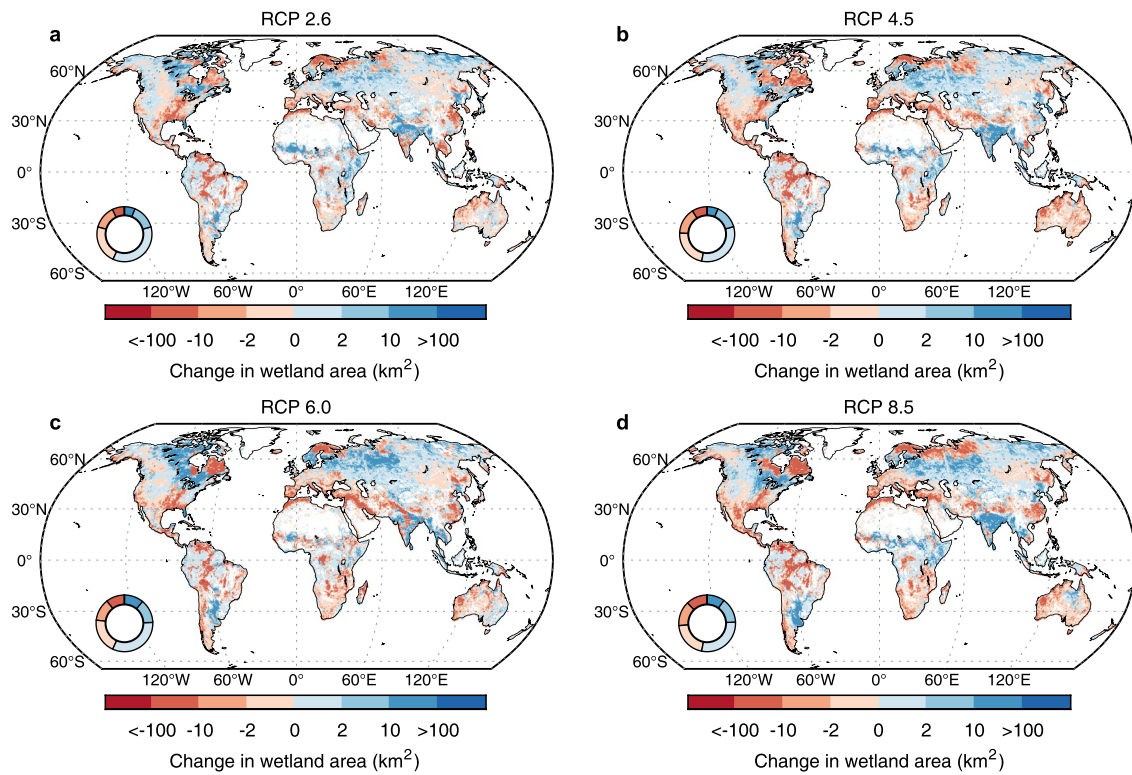
Extended Data Fig. 5 | Distributions of projected numbers of Ramsar sites with wetland gain/loss of five different cutoffs by the end of this century. **a-d** show the distributions of projected numbers of Ramsar sites with wetland gain/loss of 5%, 10%, 20%, 30%, and 50% by the end of this century under four RCP scenarios, respectively. The wider parts of distributions signify that relatively more models project that number of sites will change.



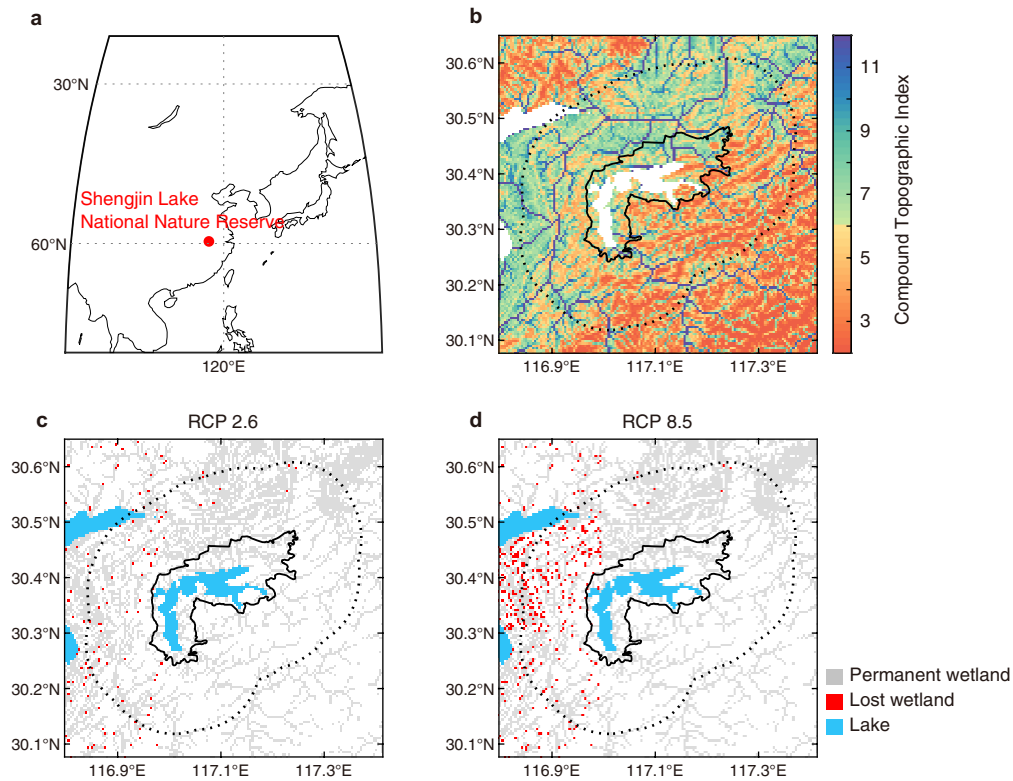
Extended Data Fig. 6 | Same as Fig. 2, but for temporal changes in numbers of inland Ramsar sites with >10% wetland loss/gain for five continents. **a, c, e, g,** and **i** show temporal changes in numbers of sites with >10% wetland loss in five continents including Africa, Asia, Europe, Latin America, and North America through the 21st century under RCP2.6, RCP8.5, and a global warming of 1.5°C and 2.0°C, while **b, d, f, h,** and **j** are for numbers of sites with >10% wetland gain in the five continents respectively.



Extended Data Fig. 7 | Wetland risk boundaries across global inland Ramsar sites by 2100. **a, c, e, g,** and **i** show multi-model mean percentage of sites shrinking by over 10% for nine criteria by the end of this century in five continents respectively under RCP2.6, and **b, d, f, h,** and **j** are for RCP8.5. C1-C9 represent nine criteria for Ramsar Site designation (Supplementary Table 1). The central angle of each criterion is determined according to the ratio of sites meeting nine criteria. The width of each annulus for each criterion is determined according to the ratio of sites with a loss of 10–20%, 20–30%, 30–50%, or more than 50% to all sites meeting this criterion. The dark grey boundary indicates the threshold of 20% of all inland sites meeting this criterion with over 10% loss.



Extended Data Fig. 8 | Projected CMIP5 ensemble mean change in wetland area for global all wetlands. a-d indicate projected CMIP5 ensemble mean change in wetland area for global all wetlands for 2081–2100 relative to the reference period 1981–2000 under RCP2.6 (13 models), RCP4.5 (18 models), RCP6.0 (9 models), and RCP8.5 (19 models) respectively.



Extended Data Fig. 9 | An example of calculating the change of Ramsar wetland. a, Spatial location of Shengjin Lake National Nature Reserve. **b**, Spatial pattern of CTI (Compound Topographic Index) for the site and the shapefile of the site and its buffer. **c, d**, Annual maximum wetland area change by 2100 from FGOALS-g2 model extracted with sub-grid CTI distribution under RCP2.6 and RCP8.5.